CrossMark

J. Fluid Mech. (2017), *vol.* 831, *pp.* 228–251. © Cambridge University Press 2017
doi:10.1017/jfm.2017.636

Boundary element methods for particles and microswimmers in a linear viscoelastic fluid

Kenta Ishimoto[1,2,3,†] **and Eamonn A. Gaffney**[3]

[1]The Hakubi Center for Advanced Research, Kyoto University, Kyoto 606-8501, Japan

[2]Research Institute for Mathematical Sciences, Kyoto University, Kyoto 606-8502, Japan

[3]Wolfson Centre for Mathematical Biology, Mathematical Institute, University of Oxford, Oxford OX2 6GG, UK

(Received 6 March 2017; revised 3 August 2017; accepted 4 September 2017; first published online 13 October 2017)

The consideration of viscoelasticity within fluid dynamical boundary element methods has traditionally required meshing over the whole flow domain. In turn, a major advantage of the boundary element method is lost, namely the need to consider only surface boundary integrals. Here, using a generalised reciprocal relation and viscoelastic force singularities, a boundary element method is developed for linear viscoelastic flows. We proceed to explore finite-deformation microswimming in a linear Maxwell fluid. We firstly deduce a finite-amplitude generalisation of a previously reported result that the flow field is unchanged between a Newtonian and linear Maxwell fluid for prescribed small-amplitude deformations. Hence Purcell's theorem holds for a linear Maxwell fluid. We proceed to consider deformation swimming in a linear Maxwell fluid given an external forcing. Boundary scattering trajectories for an exemplar squirmer approaching a surface are observed to exhibit a weak dependence on the Deborah number, while the trajectories of a sperm and monotrichous bacterium near a surface are predicted to be essentially unaffected at moderate Deborah number. In turn, the latter supports the common simplification of using Newtonian Stokes flows for studying flagellate swimming in linear Maxwell media. In addition, the motion of a magnetic helix under the influence of an external magnetic field is considered, and highlights that linear viscoelasticity can significantly impact the propagation of the helix, in turn demonstrating that even linear rheology is important to consider for forced swimmers. Finally, the presented framework requires minimalistic adjustments to Newtonian boundary element codes, enabling rapid implementation, and is more generally applicable, for instance to studies of particle interactions in active linear rheology on the microscale.

Key words: biological fluid dynamics, boundary integral methods, viscoelasticity

1. Introduction

Many physiological media exhibit non-Newtonian properties and are frequently viscoelastic due to the presence of high-molecular-weight long-chain solutes.

† Email address for correspondence: ishimoto@kurims.kyoto-u.ac.jp

https://doi.org/10.1017/jfm.2017.636 Published online by Cambridge University Press

Mammalian sperm cells migrate through the female reproductive tract, traversing highly viscoelastic liquids such as cervix mucus and cumulus cell matrix surrounding the egg (Suarez & Pacey 2006; Okabe 2013). Similarly numerous bacteria and other infectious micro-organisms are capable of penetrating the viscoelastic mucosal barrier protecting many epithelia in the body (Ribet & Cossart 2015), particularly the 30–40 m^2 of the human intestinal tract (Helander & Fandriks 2014). More generally, the ubiquity of rheological fluids in biology and physiology, together with the need for cells to move through these, has extensively motivated the study of microswimmers in a viscoelastic medium.

In modelling the impact of the viscoelasticity of physiological media on micro-swimming, a variety of constitutive relations have been considered with diverse microswimmers, as comprehensively detailed by Spagnolie (2015). For instance, one of the earliest classical studies was by Chaudhury (1979), who considered an infinite two-dimensional swimming sheet – the eponymous Taylor sheet – within a second-order fluid model. An important step enabling simple, if approximate, modelling progress for analysing the motility of flagellates such as sperm was the extension of resistive force theory to linear viscoelasticity by Fulford, Katz & Powell (1998). More recently, the explosion of interest in the theory of microswimming has led to numerous theoretical studies concerning the impact of viscoelasticity, particularly for flagellates and active filaments (Fu, Powers & Wolgemuth 2007; Fu, Wolgemuth & Powers 2008; Teran, Fauci & Shelley 2010), as well as the motility of spherical squirmers (Zhu, Lauga & Brandt 2012; Yazdi, Ardekani & Borhan 2014, 2015; Corato, Greco & Maffettone 2015). This has also been accompanied by numerous theoretical studies (e.g. Boehme & Mueller 2015; Krieger, Spagnolie & Powers 2015; Riley & Lauga 2015; Elfring & Goyal 2016), numerical investigations (e.g. Thomases & Guy 2014; Salazar, Roma & Ceniceros 2016) and experimental explorations (e.g. Godinez *et al.* 2015; Gagnon & Arratia 2016; Gomez *et al.* 2016), together with a recent extensive review (Patteson, Gopinath & Arratia 2016) and research monograph (Spagnolie 2015), where further details on this fascinating subject may be found. However, a substantive difficulty is that there appears to be no characteristic response of inertialess swimmers to non-Newtonian rheologies, with differing observations on a case-by-case basis (Curtis & Gaffney 2013; Thomases & Guy 2014; Godinez *et al.* 2015), especially for nonlinear media.

Given such complexity, there is merit in studying the simplest viscoelastic non-Newtonian constitutive relationship, namely linear viscoelasticity. Furthermore, the behaviour of particles and swimmers in such media is experimentally accessible. For particles this is illustrated by studies of micrometre-scale linear viscoelasticity (Gomez-Solano & Bechinger 2015), while a linear Maxwell model is observed to be a good approximation for the dilute methylcellulose solutions used as mucous analogues in studies of sperm motility (Smith *et al.* 2009*b*). Nonetheless, the linearly viscoelastic constitutive relation does not possess frame independence and hence it can only ever be an approximation (Spagnolie 2015). However, such corrections are degree two or higher in the fluid velocity and thus at sufficiently low velocity scales they are subdominant and can be consistently neglected at leading orders (Lauga 2014).

In addition, treating the swimmer deformation amplitude as sufficiently small also entails that the study of motility for a deforming body within a general non-Newtonian viscoelastic medium can, at leading order, be reduced to the study of swimming in a linearly viscoelastic medium (Lauga 2009, 2014). Importantly, given small deformations, the swimmer velocities and thus the swimmer dynamics

https://doi.org/10.1017/jfm.2017.636 Published online by Cambridge University Press

are identical to those obtained for Newtonian Stokes flow, as first highlighted with resistive force theory and thus slender bodies by Fulford *et al.* (1998) and more generally demonstrated for an arbitrary swimmer shape with an infinitesimally small deformation by Lauga (2014).

Thus Purcell's scallop theorem (Purcell 1977), which states that a microswimmer within a Newtonian Stokes medium cannot generate net locomotion by a reciprocal deformation (Ishimoto & Yamada 2012), holds for small-deformation inertialess swimming in linear viscoelastic media. However, it is unclear whether this generalises to finite-amplitude swimming, not least due to the correspondence between inertialess linear viscoelastic flows on the one hand and unsteady Stokes flow on the other (Xu, Forest & Klapper 2007; Feng *et al.* 2016), noting that Purcell's theorem does not hold for the latter. Hence one of our objectives below will be the consideration of Purcell's theorem for finite-deformation swimming in a linear Maxwell fluid.

More fundamentally, our aims will concern the numerical simulation of microswimmer dynamics in linear viscoelastic media. Microswimmer computations have had a long tradition, with the initial seminal paper of Gray & Hancock (1955) developing resistive force theory to enable the computation of approximate microswimming speeds by active slender bodies such as sperm. Since this time, many numerical methods have also been developed, and the boundary element method has emerged as a popular framework for computational simulation, enabling highly accurate prediction for swimmer dynamics in inertialess Newtonian flows with relatively small computational cost (Pozrikidis 1992). This framework has also been applied in the solution of viscoelastic flows, treating the viscoelastic contribution to the stress tensor as a body force, necessitating either integration or the solution of elliptic partial differential equations over the three-dimensional flow domain. Hence a major advantage of the boundary element method formalism is lost, namely the ability to reduce to the system to integral equations over surfaces, thus avoiding the numerical meshing over the whole flow field (Phan-Thien, Tran-cong & Ramia 1987; Zheng & Phan-Thien 1992; Phan-Thien & Fan 2002).

In contrast, here, our prime objective is to construct an essentially standard boundary element framework, but with the novelty that this can be used to predict linearly viscoelastic inertialess swimmer dynamics, without recourse to considering the domain of the whole flow field, by using an analogy between the solutions for Newtonian Stokes flow and linear viscoelastic flow. While a more general linear viscoelastic boundary element method is developed in appendix A, in the main text we focus on the boundary element method for a linear Maxwell fluid, which also provides a generalisation of Purcell's theorem for inertialess finite-deformation swimmers within linear Maxwell fluids.

We subsequently examine the dynamics of swimmers near boundaries, for the finite-deformation swimming of a tangential squirmer, a monotrichous (singly flagellated) bacterium and a mammalian sperm. In particular we examine the impact of linear Maxwell viscoelasticity and generalising previous works to assess whether it influences the mechanics of microswimmer boundary scattering and boundary accumulation, with the latter referring to the tendency of flagellated microswimmers to swim adjacent to surfaces.

Such studies are important in numerous contexts as exemplified by Pedley & Kessler (1992) emphasising the importance of preferential surface swimming for sperm to the fluid dynamics community. Subsequent studies on this topic have for instance greatly influenced our understanding of sperm guidance cues, such as whether surfaces are required for mammalian sperm rheotaxis, a candidate for long-range

https://doi.org/10.1017/jfm.2017.636 Published online by Cambridge University Press

sperm navigation in the female reproductive tract (Miki & Clapham 2013; Ishimoto & Gaffney 2015; Zhang *et al.* 2016). Further applications concern understanding and predicting sperm behaviours at the surface of the egg (Ishimoto, Cosson & Gaffney 2016; Ishimoto & Gaffney 2016) and in microengineered devices (Denissenko *et al.* 2012; Kantsler, Dunkel & Goldstein 2013; Nosrati *et al.* 2015), which have many prospective applications from sperm sorting to precision *in vitro* fertilisation devices. The influence of bacterial motility near surfaces for biofilm initiation was first reported at least 20 years ago (Frymier & Ford 1997). Furthermore, given the importance of biofilm formation across society, for instance with over one million annual hospital acquired infections via medical devices in the USA (Bryers 2008), there is a major impetus to understanding bacterial motility on the approach to surfaces and whether surface design can reduce colonisation (Shum *et al.* 2013). As a final exemplar, we will use boundary elements to briefly consider the motion of a magnetically driven microswimmer, once more generalising to consider a linear viscoelastic fluid, noting that such devices are under intensive development, due to their potential in novel targeted drug delivery and medical diagnostic systems (Fusco *et al.* 2014; Qiu *et al.* 2014; Qiu & Nelson 2015; Kim *et al.* 2016).

All these examples are physiological and biological in nature since numerous biological fluids, and also their mimics in experimental settings, are viscoelastic. Thus the impact of viscoelasticity on motility in such circumstances is particularly relevant and linear viscoelasticity is the simplest extension from Newtonian media, well suited to dilute long-chain molecule solutions, as verified with dilute methylcellulose for instance (Smith *et al.* 2009*b*). All such investigations are contingent on external forces and torques, due either to magnetic fields or to boundary–swimmer interactions (Frymier *et al.* 1995; Klein, Clapp & Dickinson 2003), and hence allow us to additionally highlight that external forces and torques must be handled differently in the linear viscoelastic framework developed below compared to the standard Newtonian boundary element method.

2. Problem settings

The regions external and internal to the swimmer are respectively denoted by $\Omega(t)$ and $\Omega_s(t)$, and both are functions of time t and depicted in the schematic of figure 1. The boundary of the internal region is $S = \partial\Omega_s$ and the boundary of the fluid region $\partial\Omega(t)$ is given by the union of S, the time-independent wall boundary $\partial\Omega_w$ and the far boundary at spatial infinity $\partial\Omega_\infty$, i.e. $\partial\Omega = \partial\Omega_s \cup \partial\Omega_w \cup \partial\Omega_\infty$.

Around a microswimmer, the flow is effectively inertialess and characterised by a negligible Reynolds number, with the momentum balance given by

$$\nabla \cdot \boldsymbol{\sigma} = 0, \tag{2.1}$$

where the stress tensor is defined as $\sigma_{ij} = -p\delta_{ij} + \tau_{ij}$ $(i, j = 1, 2, 3)$ for a pressure field p and a deviatoric stress tensor $\boldsymbol{\tau}$. In a Newtonian fluid, i.e. Stokes flow, one has $\boldsymbol{\tau} = 2\mu\boldsymbol{D}$, where

$$D_{ij} = \frac{1}{2}\left(\frac{\partial u_i}{\partial x_j} + \frac{\partial u_i}{\partial x_i}\right) \tag{2.2}$$

is the rate-of-strain tensor, μ is the constant viscosity of the fluid and $\boldsymbol{u}$ is the flow velocity, which also satisfies the incompressibility condition, $\nabla \cdot \boldsymbol{u} = 0$.

We impose no-slip boundary conditions on the wall and the swimmer surface. The equations of motion for the swimmer, with negligible inertia, reduce to the constraint that the swimmer experiences no net force or torque in the absence of external forcing.

https://doi.org/10.1017/jfm.2017.636 Published online by Cambridge University Press

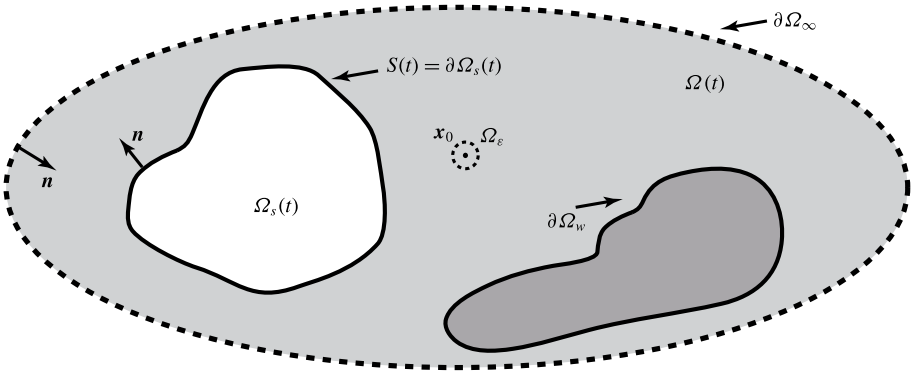


FIGURE 1. A schematic of the regions and boundaries of the system, as detailed in the text.

In this paper, we generalise to consider a linear viscoelastic medium, focusing on a Maxwell fluid in the main text, where the deviatoric stress tensor satisfies the constitutive relation

$$\mathcal{L}\boldsymbol{\tau} := \lambda\frac{\partial\boldsymbol{\tau}}{\partial t} + \boldsymbol{\tau} = 2\mu\boldsymbol{D}, \tag{2.3}$$

which approximates the flow properties of media such as dilute methylcellulose solutions (Smith *et al.* 2009*b*), with λ the elastic relaxation time. In appendix A, we also consider a more general linear viscoelastic constitutive relation,

$$\mathcal{L}\boldsymbol{\tau} = 2\mu\mathcal{M}\boldsymbol{D} := 2\mu\boldsymbol{D} + 2\mu\gamma\frac{\partial\boldsymbol{D}}{\partial t}, \tag{2.4}$$

where γ is a further response time scale.

The surface velocity of the swimmer $\boldsymbol{u}(\boldsymbol{x})$ is the combination of the linear, angular and shape deformation velocities, $\boldsymbol{U} + \boldsymbol{\Omega}\times\boldsymbol{x} + \boldsymbol{v}$. We consider a swimmer with a prescribed shape deformation, and a swimmer forced by an external magnetic field, in both cases examining the resulting prediction of the linear and angular velocities $\boldsymbol{U}$ and $\boldsymbol{\Omega}$. To proceed, we introduce two coordinate systems: the inertial reference frame with orthonormal Cartesian basis vectors $\{\boldsymbol{e}_i\}$ and the body-fixed frame with orthonormal basis vectors $\{\hat{\boldsymbol{e}}_i\}$, $i\in\{1, 2, 3\}$. The rotation from the body-fixed frame to the inertial reference coordinate frame is given by the matrix $B_{ij} = \boldsymbol{e}_i\cdot\hat{\boldsymbol{e}}_j$, and thus the deformation velocity in the reference frame is expressed by $v_i = B_{ij}(\mathrm{d}\hat{x}_j/\mathrm{d}t)$, where $\mathrm{d}\hat{x}_j/\mathrm{d}t$ is a deformation velocity in the body-fixed frame and prescribed.

3. Boundary integrals

3.1. *Reciprocal relations*

The boundary integrals associated with the boundary element method are constructed via the reciprocal relation, which imposes a constraint on two sets of solutions $(\boldsymbol{u}, \boldsymbol{\sigma})$ and $(\boldsymbol{u}', \boldsymbol{\sigma}')$ for the fluid equations within the same domain but with different boundary conditions. For Stokes flow, the reciprocal relation is (Pozrikidis 1992)

$$\frac{\partial}{\partial x_j}(u_i'\sigma_{ij} - u_i\sigma_{ij}') = 0, \tag{3.1}$$

https://doi.org/10.1017/jfm.2017.636 Published online by Cambridge University Press

with $\boldsymbol{\tau} = 2\mu \boldsymbol{D}$. However, this no longer holds for linear viscoelastic media such as the Maxwell fluid we are considering, where $\mathcal{L}\boldsymbol{\tau} = 2\mu \boldsymbol{D}$.

With the latter deviatoric stress, $\mathcal{L}\boldsymbol{\tau} = 2\mu \boldsymbol{D}$, we consider $\mathcal{L}\sigma_{ij}$ instead of σ_{ij}, and derive a similar reciprocal relation for a linearly viscoelastic fluid, given below by (3.9). The derivation is directly analogous to that presented in Pozrikidis (1992) for Newtonian flows, where further details may be found. To proceed, first consider the identity

$$u_i' \frac{\partial}{\partial x_j}(\mathcal{L}\sigma_{ij}) = \frac{\partial}{\partial x_j}(u_i' \mathcal{L}\sigma_{ij}) - \frac{\partial u_i'}{\partial x_j}\mathcal{L}\sigma_{ij}. \tag{3.2}$$

Focusing on the second term of the right-hand side above, note that the pressure term in the stress tensor does not contribute due to fluid incompressibility, so that

$$\frac{\partial u_i'}{\partial x_j}\mathcal{L}\sigma_{ij} = -\frac{\partial u_i'}{\partial x_i}\mathcal{L}p + \frac{\partial u_i'}{\partial x_j}\mathcal{L}\tau_{ij} = \frac{\partial u_i'}{\partial x_j}\mathcal{L}\tau_{ij} = 2\mu \frac{\partial u_i'}{\partial x_j} D_{ij}, \tag{3.3}$$

where the last equality holds from the constitutive relation (2.3).

Hence we have

$$u_i' \frac{\partial}{\partial x_j}(\mathcal{L}\sigma_{ij}) = \frac{\partial}{\partial x_j}(u_i' \mathcal{L}\sigma_{ij}) - 2\mu \frac{\partial u_i'}{\partial x_j} D_{ij}. \tag{3.4}$$

By analogy, we have the symmetric relation

$$u_i \frac{\partial}{\partial x_j}(\mathcal{L}\sigma_{ij}') = \frac{\partial}{\partial x_j}(u_i \mathcal{L}\sigma_{ij}') - 2\mu \frac{\partial u_i}{\partial x_j} D_{ij}'. \tag{3.5}$$

Here, noting the definition of D_{ij} and relabelling by $i \to j$ and $j \to i$, we have

$$\frac{\partial u_i'}{\partial x_j} D_{ij} = \frac{\partial u_i}{\partial x_j} D_{ij}', \tag{3.6}$$

yielding the relation

$$u_i' \frac{\partial}{\partial x_j}(\mathcal{L}\sigma_{ij}) - u_i \frac{\partial}{\partial x_j}(\mathcal{L}\sigma_{ij}') = \frac{\partial}{\partial x_j}(u_i' \mathcal{L}\sigma_{ij} - u_i \mathcal{L}\sigma_{ij}'). \tag{3.7}$$

The left-hand side of this relation, however, vanishes from the momentum-balance equations as

$$u_i' \frac{\partial}{\partial x_j}(\mathcal{L}\sigma_{ij}) = u_i' \mathcal{L} \frac{\partial \sigma_{ij}}{\partial x_j} = 0. \tag{3.8}$$

Hence we finally obtain the reciprocal relation for linearly viscoelastic flow,

$$\frac{\partial}{\partial x_j}(u_i' \mathcal{L}\sigma_{ij} - u_i \mathcal{L}\sigma_{ij}') = 0. \tag{3.9}$$

As with the Newtonian case (Pozrikidis 1992), this reciprocal relation provides the keystone for the boundary element numerical methods, as detailed below.

https://doi.org/10.1017/jfm.2017.636 Published online by Cambridge University Press

3.2. *Viscoelastic Stokeslet*

In this subsection, we consider a Stokeslet for the linear viscoelastic fluid G_{ij}, which is the Green function of this linear system and thus the velocity field when a point force at $\boldsymbol{x}_0$ is applied, defined as $\mathcal{L}(\boldsymbol{\nabla}\cdot\boldsymbol{\sigma}')_{ij} = -\delta_{ij}\delta(\boldsymbol{x}-\boldsymbol{x}_0)$, or

$$-\frac{\partial}{\partial x_i}\mathcal{L}P_j + 2\mu\nabla^2 G_{ij} = -\delta_{ij}\delta(\boldsymbol{x}-\boldsymbol{x}_0), \tag{3.10}$$

where P_j is the associated pressure and the singularity location, $\boldsymbol{x}_0$, in general may be a function of time. We can therefore express the Stokeslet for the linear viscoelastic fluid by the solutions for the Newtonian Stokes flow,

$$G_{ij} = G^S_{ij} \quad \text{and} \quad \mathcal{L}P_j = P^S_j, \tag{3.11a,b}$$

with the superscript S referring to Stokes flow.

Let the constant vector $\boldsymbol{q}$ be a force strength, and introduce a set of solutions for the linear viscoelastic fluid flow,

$$u'_i = \frac{1}{8\pi\mu}G_{ij}(\boldsymbol{x},\boldsymbol{x}_0)q_j, \quad p' = \frac{1}{8\pi}P_j q_j, \quad \sigma'_{ij} = \frac{1}{8\pi}T_{ijk}q_k, \tag{3.12a–c}$$

whereby we have

$$\mathcal{L}\sigma'_{ij} = -(\mathcal{L}P_m)q_m\delta_{ij} + 2\mu D'_{ij} = -\frac{1}{8\pi}P^S_m q_m + \frac{1}{8\pi}\left(\frac{\partial G^S_{ip}}{\partial x_j} + \frac{\partial G^S_{jp}}{\partial x_i}\right)q_p. \tag{3.13}$$

This is equivalent to

$$\mathcal{L}\sigma'_{ij} = \sigma'^S_{ij}, \tag{3.14}$$

where σ'^S_{ij} is the stress tensor for the Newtonian Stokes flow, given by $\sigma'^S_{ij} = (1/8\pi)T^S_{ijp}q_p$. Thus (3.14) can be rephrased as

$$\mathcal{L}T_{ijp} = T^S_{ijp}. \tag{3.15}$$

In principle there is an undetermined freedom regarding the initial condition. We thus assume the flow is stationary at initial time, t_0, and then in turn σ'_{ij} is uniquely specified as the operator $\mathcal{L}$ is linear.

More generally, note that, in developing a boundary element method, one is constructing the flow field from the linear superposition of singularity solutions (Pozrikidis 1992), and the choice of singularity solutions is the same as choosing a basis for a representation of the velocity field. Thus here we are using Newtonian velocity singularities, since $G_{ij} = G^S_{ij}$, but the associated singularity pressure and stress fields are now more complex, and given by $\mathcal{L}P_j = P^S_j$, $\mathcal{L}T_{ijp} = T^S_{ijp}$, to ensure the reciprocal theorem holds. The latter in turn enables the construction of the boundary element method to find the decomposition of the flow field into singularity solutions even with linear viscoelasticity. However, the pressure and stress fields do not enter the final formalism and thus the net influence of linear viscoelasticity only significantly arises in the force and torque balances for the swimmer, which are, at most, modified in a simple manner. In turn, this enables a rapid adaptation of standard boundary element codes to study swimming in linearly viscoelastic media, as we shall derive and detail below.

https://doi.org/10.1017/jfm.2017.636 Published online by Cambridge University Press

3.3. *Boundary integral equations*

Based on the relations derived above, we are in a position to formulate the viscoelastic boundary integral equations, starting with the reciprocal relation (3.9). Substitution of the velocity and the stress of the point force flow $(\boldsymbol{u}', \boldsymbol{\sigma}')$, obtained in (3.11) and (3.15), into the reciprocal relation gives us the relation for the velocity and the stress of our swimmer problem $(\boldsymbol{u}, \boldsymbol{\sigma})$ as

$$\frac{\partial}{\partial x_j}\left(\frac{1}{8\pi\mu}G^S_{ip}q_p(\mathcal{L}\sigma_{ij}) - \frac{1}{8\pi}u_i T^S_{ijp}q_p\right) = 0. \tag{3.16}$$

This relation is integrated over the fluid region except for a small sphere of radius ϵ around the singular point $\boldsymbol{x}_0$, $\Omega\backslash\Omega_\epsilon$, as depicted in figure 1. Noting the zero-velocity constraint on the wall boundary and at infinity, we have

$$\int_{S\cup\partial\Omega_\epsilon}(G^S_{ip}(\mathcal{L}\sigma_{ij}) - \mu u_i T^S_{ipj})\boldsymbol{n}_j\,\mathrm{d}S = 0, \tag{3.17}$$

where the vector $\boldsymbol{n}_j$ denotes the outward normal of the surface region, as in figure 1. The time derivative implicit within the operator $\mathcal{L}$ on the swimmer surface S should be clarified. We take a larger region that covers the surface S, with separation $\delta > 0$ from it, and consider the time derivatives for the variables outside S but in the larger region, where the derivative is unambiguously defined, before taking the limit of $\delta \to 0$.

Exactly as in the Newtonian case (Pozrikidis 1992, p. 26), the integral over $\partial\Omega_\epsilon$ converges to $8\pi\mu u_p(\boldsymbol{x}_0)$ in the limit of $\epsilon \to 0$, yielding the viscoelastic boundary integral equation,

$$u_p(\boldsymbol{x}_0) = -\frac{1}{8\pi\mu}\int_S G^S_{ip}(\mathcal{L}\sigma_{ij})\boldsymbol{n}_j\,\mathrm{d}S + \frac{1}{8\pi}\int_S u_i T^S_{ipj}\boldsymbol{n}_j\,\mathrm{d}S. \tag{3.18}$$

The first of these integrals is known as a single-layer boundary integral, while the second is known as a double-layer boundary integral. The latter requires care in its treatment, as the integrand is singular, and not just weakly singular. The evaluation of these integrals in the Newtonian case is fully documented (e.g. Pozrikidis 1992) and immediately generalises to (3.18), as the double-layer singularity, T^S_{ijk}, is the Newtonian singularity. However, we do not follow this approach here. Instead we explicitly assume the swimmer volume is invariant. Then it is much simpler to eliminate the second integral of (3.18), and write $u_p(\boldsymbol{x}_0)$ in terms of only a single-layer boundary integral, as is well known for the Newtonian boundary element method (Pozrikidis 1992) and as we now demonstrate for linear viscoelasticity.

To proceed, let * denote variables associated with a fictitious virtual flow within the interior of the swimmer $\Omega_s(t)$ on making the supposition that the swimmer interior is constituted from the same linear viscoelastic medium as external to the swimmer. For example, let $\boldsymbol{u}^*$ denote the velocity field of this internal swimmer flow; its incompressibility immediately requires the restriction that swimmer volume is invariant. Given this, the same reciprocal relation (3.9) then holds in the interior region Ω_s, and integrating over this region yields

$$0 = \int_{\Omega_s}\frac{\partial}{\partial x_j}(G^S_{ip}\mathcal{L}\sigma^*_{ij} - \mu u^*_i T^S_{ipj})\,\mathrm{d}V = \int_S (G^S_{ip}\mathcal{L}\sigma^*_{ij} - \mu u_i T^S_{ipj})\boldsymbol{n}_j\,\mathrm{d}S, \tag{3.19}$$

after using the divergence theorem and continuity of velocity at the cell surface. The vector $\boldsymbol{n}_j$ again denotes the outward normal to the swimmer surface. We use the

https://doi.org/10.1017/jfm.2017.636 Published online by Cambridge University Press

solutions $(\boldsymbol{u}', \boldsymbol{\sigma}')$ and $(\boldsymbol{u}'^*, \boldsymbol{\sigma}'^*)$ for a point force at $\boldsymbol{x}_0$ outside Ω_s, and substituting (3.19) into (3.18) we have the single-layer integral equation,

$$u_p(\boldsymbol{x}_0) = -\frac{1}{8\pi\mu}\int_S G^S_{ip}(\boldsymbol{x}, \boldsymbol{x}_0)\mathcal{L}(\sigma_{ij}(\boldsymbol{x}) - \sigma^*_{ij}(\boldsymbol{x}))\boldsymbol{n}_j \,\mathrm{d}S_{\boldsymbol{x}}. \tag{3.20}$$

We therefore find the same expression for the single-layer integral equation as in the Newtonian case with

$$f^{VE}_i = \mathcal{L}(\sigma_{ij} - \sigma^*_{ij})\boldsymbol{n}_j \tag{3.21}$$

giving the linear viscoelastic generalisation of the jump in the traction between the exterior and interior flows. When we take the limit of $\boldsymbol{x}_0$ approaching the swimmer surface S, we obtain the single-layer boundary integral equation for the surface velocity,

$$u_p(\boldsymbol{x}_0) = -\frac{1}{8\pi\mu}\int_S G^S_{ip}(\boldsymbol{x}, \boldsymbol{x}_0) f^{VE}_i(\boldsymbol{x}) \,\mathrm{d}S_{\boldsymbol{x}}. \tag{3.22}$$

3.4. *Force and torque balance equations*

For the swimmer problem, we seek the linear and angular velocities $\boldsymbol{U}$ and $\boldsymbol{\Omega}$ of the swimmer when its deformation is given. In addition to the no-slip boundary condition on the swimmer surface, equation (3.22), the equations of motion for the swimming body are required to close the system. At negligible Reynolds number, these reduce to the conditions of zero force and zero torque on the swimmer, given there are no external forces and torques. The zero-force condition,

$$\int_{S(t)} \sigma_{ij}\boldsymbol{n}_j \,\mathrm{d}S = 0, \tag{3.23}$$

needs to be expressed in terms of the viscoelastic traction jump, $\boldsymbol{f}^{VE}$. From the momentum balance (2.1) and the divergence theorem, we have

$$\mathcal{L}\int_{S(t)} \sigma_{ij}\boldsymbol{n}_j \,\mathrm{d}S = -\mathcal{L}\int_{\partial\Omega_w\cup\partial\Omega_\infty} \sigma_{ij}\boldsymbol{n}_j \,\mathrm{d}S = -\int_{\partial\Omega_w\cup\partial\Omega_\infty} (\mathcal{L}\sigma_{ij})\boldsymbol{n}_j \,\mathrm{d}S, \tag{3.24}$$

with the temporal operator in $\mathcal{L}$ commuting with integration on the right-hand side, as the integration domain is time-invariant. Using the momentum-balance relation and the divergence theorem once more gives the general commutation of the surface integral and the linear operator $\mathcal{L}$:

$$\mathcal{L}\int_{S(t)} \sigma_{ij}\boldsymbol{n}_j \,\mathrm{d}S = \int_{S(t)} (\mathcal{L}\sigma_{ij})\boldsymbol{n}_j \,\mathrm{d}S. \tag{3.25}$$

Furthermore, note that for the virtual interior flow

$$\int_{S(t)} (\mathcal{L}\sigma^*_{ij})\boldsymbol{n}_j \,\mathrm{d}S = \int_{\Omega_s} \frac{\partial}{\partial x_j}(\mathcal{L}\sigma^*_{ij}) \,\mathrm{d}V = \int_{\Omega_s} \mathcal{L}\frac{\partial \sigma^*_{ij}}{\partial x_j} \,\mathrm{d}V = 0, \tag{3.26}$$

and hence we obtain the relation

$$\mathcal{L}\int_{S(t)} \sigma_{ij}\boldsymbol{n}_j \,\mathrm{d}S = \int_{S(t)} \mathcal{L}(\sigma_{ij} - \sigma^*_{ij})\boldsymbol{n}_j \,\mathrm{d}S = \int_{S(t)} f^{VE}_i \,\mathrm{d}S. \tag{3.27}$$

https://doi.org/10.1017/jfm.2017.636 Published online by Cambridge University Press

The zero-force condition (3.23) therefore entails

$$\int_{S(t)} f_i^{VE}\,\mathrm{d}S = 0, \tag{3.28}$$

for all time.

The zero-torque condition

$$\int_{S(t)} \epsilon_{ipq} x_p \sigma_{qj} \boldsymbol{n}_j\,\mathrm{d}S = 0 \tag{3.29}$$

is rewritten in a similar manner. Applying the operator $\mathcal{L}$ to this integral together with the divergence theorem gives us

$$\mathcal{L}\int_{S(t)} \epsilon_{ipq} x_p \sigma_{qj} \boldsymbol{n}_j\,\mathrm{d}S = -\mathcal{L}\int_{\partial\Omega_w\cup\partial\Omega_\infty} \epsilon_{ipq} x_p \sigma_{qj} \boldsymbol{n}_j\,\mathrm{d}S + \mathcal{L}\int_{\Omega(t)} \frac{\partial}{\partial x_j}(\epsilon_{ipq} x_p \sigma_{qj})\,\mathrm{d}V. \tag{3.30}$$

The integrand of the volume integral vanishes due to the momentum balance and the symmetry of the stress tensor, with the same reasoning applying to the internal flow relationship:

$$\int_{S(t)} \epsilon_{ipq} x_p (\mathcal{L}\sigma^*_{qj}) \boldsymbol{n}_j\,\mathrm{d}S = \int_{\Omega_s} \frac{\partial}{\partial x_j}(\epsilon_{ipq} x_p (\mathcal{L}\sigma^*_{qj}))\,\mathrm{d}V = 0. \tag{3.31}$$

Thus the integral (3.30) reduces to

$$\mathcal{L}\int_{S(t)} \epsilon_{ipq} x_p \sigma_{qj} \boldsymbol{n}_j\,\mathrm{d}S = \int_{S(t)} \epsilon_{ipq} x_p (\mathcal{L}\sigma_{qj}) \boldsymbol{n}_j\,\mathrm{d}S = \int_{S(t)} \epsilon_{ipq} x_p f_q^{VE}\,\mathrm{d}S, \tag{3.32}$$

which yields the zero-torque condition

$$\int_{S(t)} \epsilon_{ipq} x_p f_q^{VE}\,\mathrm{d}S = 0. \tag{3.33}$$

Equations (3.22), (3.28) and (3.33) complete the swimmer problem, which gives us the swimmer velocities, $\boldsymbol{U}$ and $\boldsymbol{\Omega}$. This set of equations has the same form as the Newtonian case, though the corresponding tractions are not identical. Thus the swimmer velocities, and therefore the swimmer trajectories, are identical to those in the Newtonian Stokes flow for any finite prescribed shape deformation, regardless of the linear viscoelasticity of the Maxwell medium. Hence Purcell's scallop theorem holds for finite-deformation swimming in a linear Maxwell fluid.

4. Swimmer–wall interactions

As we have seen, the swimming trajectory in a linear Maxwell fluid is identical to that in the Newtonian Stokes fluid, if no external forces and torques are applied. However, once the swimmer experiences such forces, the motion may be affected by the fluid viscoelasticity. As detailed in the introduction, the behaviour of swimmers near a surface is a very important subject of study in numerous contexts, and thus below we consider swimming near a flat plane wall.

https://doi.org/10.1017/jfm.2017.636 Published online by Cambridge University Press

4.1. *Wall interaction*

When a swimmer is less than submicrometre length scales from a boundary, we can no longer neglect molecular-based swimmer–wall interactions. While there are no comprehensive data on such interactions, it has been reported that the wall interaction of *Escherichia coli* can be attractive or repulsive according to the solutes present (Klein *et al.* 2003) and on a length scale of approximately 100 nm. One also regularly observes that sperm easily stick to naked glass, requiring the use of dilute albumin to enable swimming adjacent to coverslips (Smith *et al.* 2009*b*). Also, particular proteins distributed on the sperm head can bind to biological surfaces such as the epithelium of the mammalian oviduct and the zona pellucida (Okabe 2013; Suarez 2016).

Hence, as used in previous studies (Ishimoto *et al.* 2016; Ishimoto & Gaffney 2016) and assuming conditions that the swimmer does not bind to the surface, we introduce a repulsive interaction potential for a repulsive force per unit area between the wall and the swimmer surface at the position $\boldsymbol{x}$. This is given via

$$\boldsymbol{f}_{wall}(\boldsymbol{x}) = g\frac{\mathrm{e}^{-r/d}}{1-\mathrm{e}^{-r/d}}\boldsymbol{e}_r, \tag{4.1}$$

where r is the distance from the surface and $\boldsymbol{e}_r$ denotes the outward normal of the wall, which we consider hereafter as a no-slip rigid infinite plane boundary, and the constants g and d represent the force strength and the force length scale, respectively.

The force and torque balance equations, (3.28) and (3.33), thus need to be modified to accommodate this wall interaction. The force balance is given by

$$\int_S \sigma_{ij}\boldsymbol{n}_j \,\mathrm{d}S + \int_S (f_{wall})_i \,\mathrm{d}S = 0. \tag{4.2}$$

Applying the operator $\mathcal{L}$ to both sides, and using (3.25) and arguments analogous to those presented in the previous section, we have

$$\int_S f_i^{VE} \,\mathrm{d}S_{\boldsymbol{x}} + \mathcal{L}\int_S (f_{wall})_i \,\mathrm{d}S = 0. \tag{4.3}$$

The torque balance equation is similarly obtained, to give

$$\int_S \epsilon_{ipq}x_p f_q^{VE} \,\mathrm{d}S_{\boldsymbol{x}} + \mathcal{L}\int_S \epsilon_{ipq}x_p (f_{wall})_q \,\mathrm{d}S = 0. \tag{4.4}$$

Note that the singularity solution used in the boundary integral equation (3.18) or (3.22) satisfies appropriate boundary conditions of no slip on $\partial\Omega_w$ and zero for $\partial\Omega_\infty$. Hence the integral kernel in the presence of a wall, G_{ip}^S, is that of the Blakelet (Blake 1971), which we employ for numerical computation below. Finally, observe that the structure of the equations is that of the standard, Stokes flow, boundary element method, enabling rapid generalisation of existing boundary element numerical libraries for linear viscoelastic calculations.

4.2. *Numerical implementation*

Here we use the single-layer formulation for microswimming problems (Ishimoto & Gaffney 2014*a*,*b*) to consider deformation swimming in a linear Maxwell fluid with a constitutive relation given by $\mathcal{L}\boldsymbol{\tau} = 2\mu\boldsymbol{D}$. This requires solving the linear set of equations (3.22), (4.3) and (4.4), in which the traction $\boldsymbol{f}^{VE}(\boldsymbol{x})$ and the velocities $\boldsymbol{U}$

https://doi.org/10.1017/jfm.2017.636 Published online by Cambridge University Press

and $\boldsymbol{\Omega}$ are unknown but the swimmer deformation $\boldsymbol{v}$ is given. The only difference from the Newtonian case is the additional operator $\mathcal{L}$ in the force and torque balance equations (4.3) and (4.4). The swimmer surface S is discretised by N triangular meshes, and the surface integrals are numerically performed by Gaussian quadratures supported by the BEMLIB library (Pozrikidis 2002). The resulting $3N + 6$ coupled linear equations are then solved via an LU decomposition. The time marching of the system is implemented by the Heun method (Smith *et al.* 2009*a*). As exemplars, we consider a spherical tangential squirmer, a bacterial swimmer and a sperm-like swimmer, as detailed in the following sections.

4.3. *Spherical tangential squirmer*

The first example swimmer is a spherical squirmer, which is driven via a tangential surface velocity profile on its surface. In particular, we consider a sphere of radius a with its centre a height h above an infinite plane wall at $z = 0$, and introduce a swimmer orientation vector $\boldsymbol{d}$ within the xz plane, making an angle φ with the plane wall; see figure 2. The surface velocity profile is given by

$$u_\theta(\theta) = V \sin\theta, \tag{4.5}$$

where the angle θ is measured from the orientation vector $\boldsymbol{d}$, as also depicted in figure 2. This swimmer is also known as a neutral squirmer (Ishikawa, Simmons & Pedley 2006), and is repelled by the wall in the absence of wall interactions (Ishimoto & Gaffney 2013).

The sphere radius and the surface velocity are non-dimensionalised to a unit radius and a non-dimensional velocity $V = 3/2$. Owing to this scaling, the non-dimensional swimming velocity in the absence of a wall becomes unity. The number of mesh elements on the swimmer surface is $N = 2048$, and the meshes are iteratively generated by the BEMLIB library accompanying Pozrikidis (2002). The discretisation for each time step is given by $\Delta t = 1/400$, and the constants of the wall interactions are set as $(g\mu/T,\, d/a) = (400,\, 1/50)$. The large scale of the interaction strength entails the repulsive force is very large once the swimmer is in the vicinity of the wall, while the small interaction length scale entails that the swimmer has to be very close to the wall to experience the repulsive force.

We performed numerical computations, changing the initial angle of attack and the Deborah number, which is the non-dimensional relaxation time, given by $De = \lambda/T$, where $T = 3a/2V$ is the characteristic time scale of this system. In figure 2(*b*), the computed trajectories of the squirmer are plotted for an initial angle of attack $\varphi_{init} = 0.2\pi$ with the Deborah numbers $De \in \{0,\ 1,\ 10\}$. It is found that the viscoelasticity weakly increases the surface repulsion and weakly influences the scattering angle and the duration that the swimmer remains near the wall. In particular, on varying the initial angles of attack for these swimmers, the relation between the initial and final scattering angles $(\varphi_{init},\, \varphi_{fin})$ is plotted in figure 2(*c*). In these simulations, the swimmer is initially located at $(x,\, z) = (0,\, 5)$ and the final angles are obtained from the trajectory only once the simulation times reaches $50T$, so that the swimmer is in the very far field of the wall. In the plots of figure 2(*c*), for the cases with shallow initial angles, the swimmer does not approach the area with wall interactions, and thus the scattering angles are well explained by the far-field point singularity theory,

$$\varphi_{fin} = \sqrt{\varphi_{init}^2 + 1/64}, \tag{4.6}$$

https://doi.org/10.1017/jfm.2017.636 Published online by Cambridge University Press

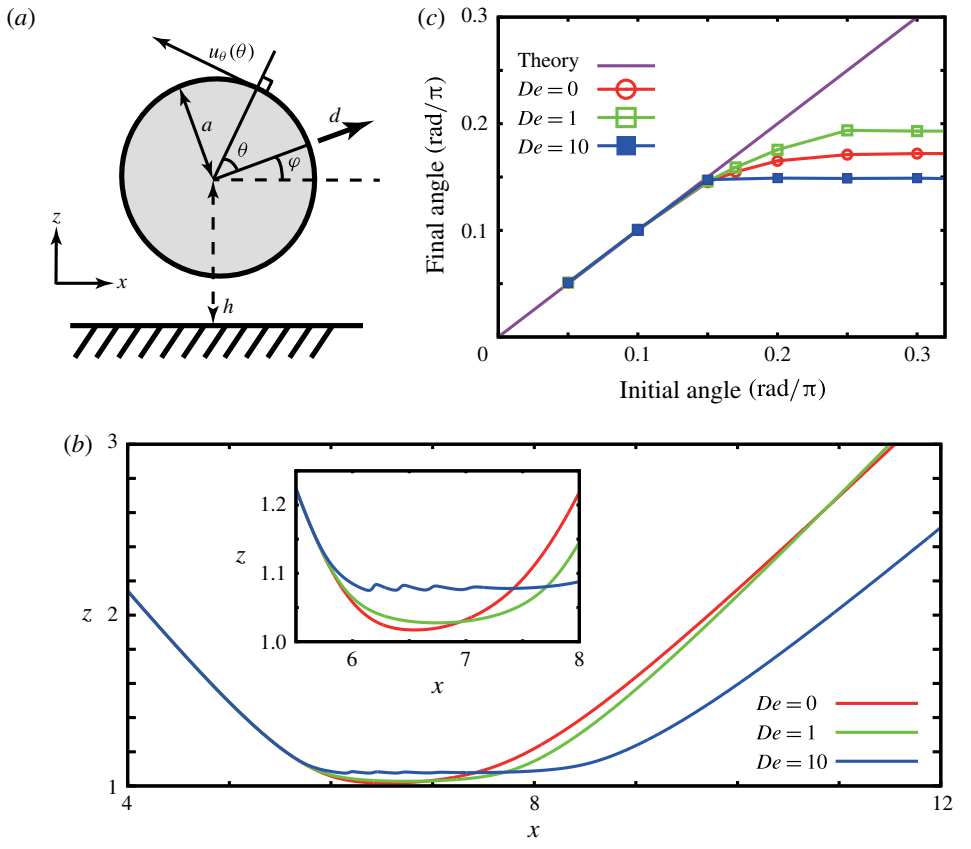


FIGURE 2. (Colour online) (*a*) A schematic of the spherical squirmer. (*b*) Example swimmer trajectories near a wall with an enlarged view shown in the inset. (*c*) Relation of the initial and final scattering angles for wall scattering, including Newtonian theoretical predictions for shallow scattering.

provided by Spagnolie & Lauga (2012). Nonetheless, as the initial angle steepens, the final angles deviate from the shallow-angle theoretical prediction and vary non-monotonically with the Deborah number.

4.4. *Bacterial swimmer*

The second example is a monotrichous bacterial swimmer, which is known to accumulate near a no-slip wall (Berke *et al.* 2008) and numerical simulations have shown that hydrodynamic interactions are sufficient to explain even the subtle aspects of this accumulation behaviour (Giacché, Ishikawa & Yamaguchi 2010; Goto, Nakai & Aoki 2010; Shum, Gaffney & Smith 2010). Hence this example examines the extent to which viscoelastic effects may alter stable swimming near a surface, as opposed to the scattering of the previous example.

The virtual bacterium consists of a spheroidal cell body, whose polar radius and equatorial radius are, respectively, a_1 and a_2, together with a single cylindrical flagellum of length L and radius r (figure 3*a*). Following Shum *et al.* (2010), the flagellum waveform is taken to be a helical wave, and the centreline of the flagellum

https://doi.org/10.1017/jfm.2017.636 Published online by Cambridge University Press

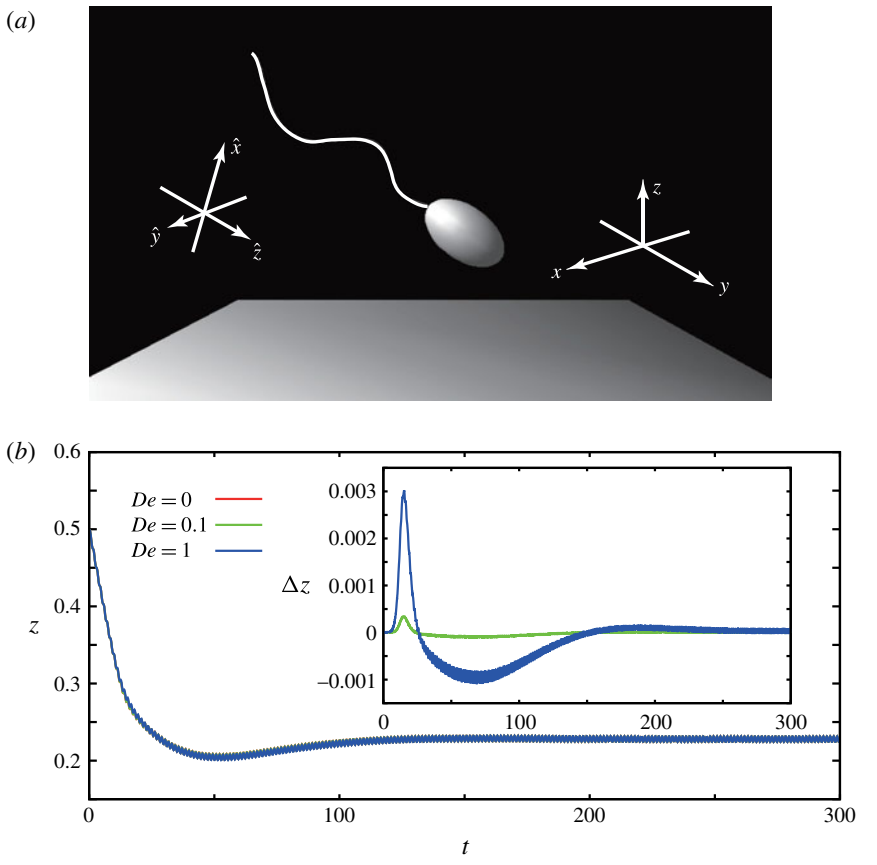


FIGURE 3. (Colour online) (*a*) A schematic of the monotrichous bacterial swimmer with its flagellum, together with the axes of the inertial and body-fixed reference frames and the underlying no-slip wall. (*b*) The time evolution of the separation distance from the proximal flagellum to the wall, with differences of z from the $De = 0$ case depicted for $De = 0.1$ and $De = 1$ in the inset.

is given in terms of the body-fixed coordinates $(\hat{x}(\hat{z}, t), \hat{y}(\hat{z}, t), \hat{z})$ by

$$\hat{x} = A(1 - \mathrm{e}^{-k_E^2 \hat{z}^2}) \cos(k\hat{z} + \omega t), \tag{4.7}$$

$$\hat{y} = A(1 - \mathrm{e}^{-k_E^2 \hat{z}^2}) \sin(k\hat{z} + \omega t), \tag{4.8}$$

where A is the amplitude of the helix, k is the wavenumber and $\omega = 2\pi/T$ is the angular velocity in terms of the time period T. The parameter k_E governs the scale of the initial increase in the flagellar envelope as the flagellum leaves its junction with the cell body at $\hat{\boldsymbol{x}} = \boldsymbol{0}$. The functions (4.7) and (4.8) are defined for $\hat{z} \in [\hat{z}_{end}, 0]$, where the coordinate of the flagellar distal end $\hat{z}_{end} < 0$ is given by

$$L = \int_{\hat{z}_{end}}^{0} \sqrt{1 + \left(\frac{\mathrm{d}\hat{x}}{\mathrm{d}\hat{z}}\right)^2 + \left(\frac{\mathrm{d}\hat{y}}{\mathrm{d}\hat{z}}\right)^2}\, \mathrm{d}\hat{z}. \tag{4.9}$$

In the simulation, the parameters of the model bacterium are those of optimal power efficiency, as obtained by Shum *et al.* (2010) and given by $a_1/L = 0.154$,

https://doi.org/10.1017/jfm.2017.636 Published online by Cambridge University Press

$a_2/L = 0.0922$, $k_E L = 10.0$, $A/L = 0.079$, $kL/2\pi = 1.953$ and $r/L = 0.003$. The system is non-dimensionalised using the flagellum length for the length scale L, the flagellum rotation period for the time scale T and the medium viscosity for the force scale, such that the non-dimensional viscosity is unity. Note however that, for the virtual bacterial model discussed by Shum *et al.* (2010), the flagellum rotates with a constant applied torque at its proximal end. In this study, in contrast, the flagellum motion is fully prescribed in the body-fixed frame by the functions (4.7) and (4.8), and the bacterial motion is therefore subject to the same kinematical problem as the squirmer case.

The surface meshes are generated as in Shum *et al.* (2010), with the head mesh constructed in the same way as the squirmer, with a subsequent stretching to generate the ellipsoidal head shape. The flagellum is meshed as a hexagonal tube with hemispherical caps at the ends, noting a small cell–flagellum gap is introduced in practice to numerically accommodate the relative motion of these surfaces as in previous studies (Shum *et al.* 2010; Ishimoto & Gaffney 2014*a*). The total number of mesh elements on the swimmer surface is set to $N = 494$, and the discretisation for each time step is given by $\Delta t = 1/400$. The constants of the wall interactions are once more set to $(g\mu/T, d/L) = (400, 1/50)$.

We conducted numerical simulations with different Deborah numbers $De = \lambda/T \in \{0, 0.1, 1\}$. Note that at high Deborah numbers the forces and torques acting on the flagellum can differ substantially relative to the Newtonian case, and therefore the flagellar motion may change even if the internal torque generation is invariant. In such a highly elastic medium, the prescribed motion is in fact likely to be altered. In contrast to the previous idealised example of a squirmer, which we assumed can always maintain the prescribed deformation even with large elastic forces, here we focus on moderate values of the Deborah number. In figure 3(*b*), the time evolution of the distance from the wall boundary and the flagellar proximal end is plotted, and the differences are relatively minor, as particularly emphasised by the inset. The swimmer is initially located so that the flagellar proximal end is at $\boldsymbol{x} = (0, 0, 0.5)$ and its initial angle of attack relative to the wall is 0.2π. After the swimmer reaches the region where the wall interaction is significant, the cell body rotates away from the surface and the cell subsequently relaxes to stable swimming adjacent to the wall.

4.5. *Sperm-like swimmer*

The third example swimmer is based on the morphology of a sperm, as illustrated in figure 4(*a*). Sperm in particular can be significantly affected by steric interactions when a sudden change in surface topography induces scattering (Kantsler *et al.* 2013). In addition, it is theoretically predicted that steric interactions significantly influence the behaviour of a sperm cell near a boundary (Montenegro-Johnson, Gadelha & Smith 2015; Ishimoto & Gaffney 2015, 2016) where, in the latter citation, we examine the impact of viscoelasticity on beating cells adhered to a wall. Hence, here we consider how viscoelasticity impacts sperm swimming trajectories near a wall, which necessitates a viscoelastic boundary element method in the absence of the simplification associated with cell attachment.

The virtual sperm-like swimmer has a flattened ellipsoidal head of human sperm and a cylindrical tail flagellum of length L and radius r. The head and tail morphologies are motivated by the human sperm geometrical model provided in Ishimoto & Gaffney (2016), with a prescribed flagellar waveform that is an ellipsoidal helical wave (Smith

https://doi.org/10.1017/jfm.2017.636 Published online by Cambridge University Press

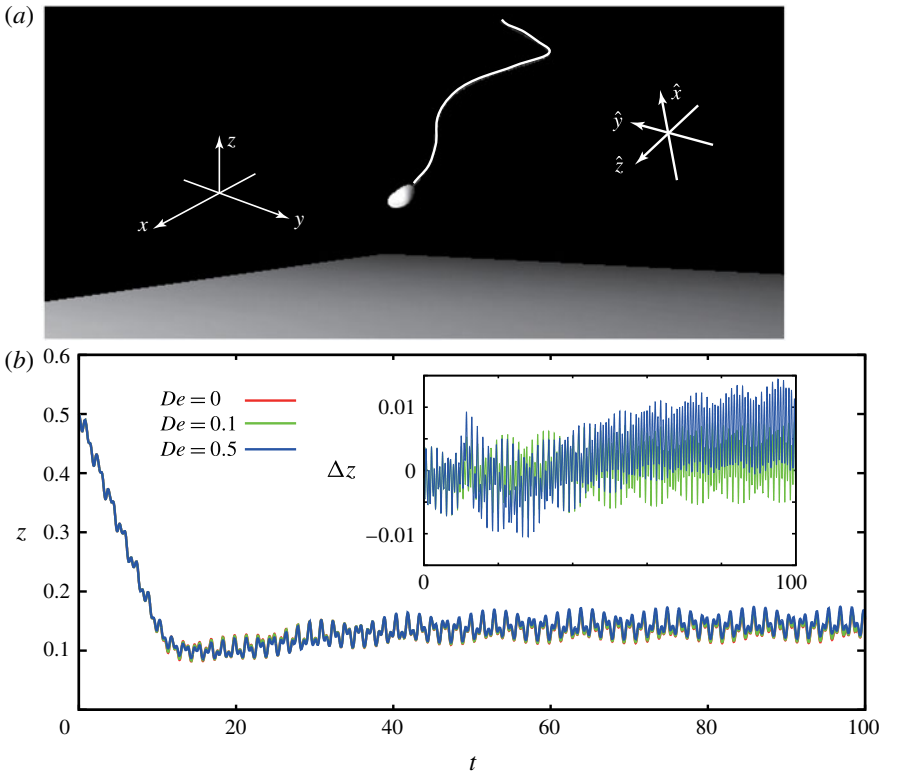


FIGURE 4. (Colour online) (*a*) A schematic of the sperm-like swimmer with its flagellum above a no-slip plane boundary, together with body-fixed and inertial reference frame axes. (*b*) The time evolution of the separation distance of the cell body–flagellum junction from the wall, with differences of z from the Newtonian case shown for $De = 0.1$ and $De = 0.5$ in the inset.

et al. 2009*a*), with an ellipsoidal cone envelope. The centreline of the flagellum is again defined as a function of $\hat{z} \in [\hat{z}_{end}, 0]$, via

$$\hat{x} = \alpha A|\hat{z}| \cos(k\hat{z} + \omega t), \tag{4.10}$$

$$\hat{y} = A|\hat{z}| \sin(k\hat{z} + \omega t), \tag{4.11}$$

where the parameter α represents the major to minor aspect ratio of the elliptical cross-section through the enveloping cone of the flagellar beat, and $\hat{z}_{end} < 0$ satisfies the fixed length constraint given by (4.9). The parameters used in the simulation are taken from Ishimoto & Gaffney (2016), where morphological justification is provided; in particular we have $\alpha = 0.2$, $A/L = 0.2$, $kL/2\pi = 1.5$ and $r/L = 0.0223$. As with the bacterial swimmer, the system is non-dimensionalised using the flagellum length L for the length scale, the beat period T for the time scale and the medium viscosity for the force scale, such that the non-dimensional viscosity is unity.

The surface meshes are generated in a similar manner to the bacterial swimmer, details of which are provided in our previous studies (Ishimoto & Gaffney 2014*a*, 2016). The total number of mesh elements on the swimmer surface is again $N = 494$, and the discretisation for each time step is given by $\Delta t = 1/1600$. The constants of the

https://doi.org/10.1017/jfm.2017.636 Published online by Cambridge University Press

wall interactions are set to $(g\mu/T, d/L) = (400, 1/50)$ while the swimmer is initially located so that the head–flagellum junction is at $\boldsymbol{x} = (0, 0, 0.5)$ and its angle of attack to the wall is 0.2π.

The results of similar numerical simulations with different Deborah numbers $De = \lambda/T \in \{0, 0.1, 0.5\}$ are shown in figure 4(*b*) at integer times, or every beat cycle, with enlarged views inset. As with the bacterium, we do not consider large elasticity, because the prescribed waveform is unlikely to be conserved; instead, we consider moderate Deborah numbers once more. In figure 4(*b*), the time evolution of the distance between the wall and the head–flagellum junction is plotted, and the differences are relatively minor here too, as emphasised by the inset. Similarly to the bacterial case, the swimmer rotates on encountering the wall interactions, but the sperm head is slightly directed towards the wall. Furthermore, when the cell trajectory has asymptoted to boundary swimming, the conical envelope of the flagellum has rotated sufficiently downwards so as to induce intermittent wall interactions during the beat period. However, despite the fact that these interactions differ in the contribution to the momentum balances for the cell according to medium rheology, the actual trajectory of the sperm is not significantly altered on comparing swimming in a Newtonian fluid to that in a linear Maxwell fluid.

5. Magnetic swimmer

For a different application of the linear viscoelastic formulation, we consider a neutrally buoyant rigid helix with a permanent magnetisation, which can be induced to swim via an external magnetic field, as motivated by studies of externally guided helical microswimmers for many applications such as drug delivery (Qiu & Nelson 2015).

5.1. *Model*

The magnetic swimmer is taken to be a rigid helix of length L and radius r, as considered in the section discussing the bacterial swimmer and depicted in figure 3. The centreline of the helix is given in terms of the body-fixed coordinates $(\hat{x}(\hat{z}), \hat{y}(\hat{z}))$ by

$$\hat{x} = A\cos(k\hat{z}) \quad \text{and} \quad \hat{y} = A\sin(k\hat{z}), \tag{5.1a,b}$$

where A is the radius of the helix and k is the wavenumber, with the latter giving the pitch of the helix. The $\hat{z}$ coordinate ($\hat{z} \in [\hat{z}_{end}, 0]$) is related to the arclength via the fixed length constraint given by (4.9).

We assume the swimmer is a hard magnet with a fixed magnetisation $\boldsymbol{M} = M_0\hat{\boldsymbol{e}}_x$ along the body-fixed $\hat{x}$ axis. Therefore the helix experiences a force and torque in the presence of a magnetic flux density $\boldsymbol{B}$ given by (Qiu & Nelson 2015)

$$\boldsymbol{F}_{ext} = C_0(\boldsymbol{M}\cdot\nabla)\boldsymbol{B}, \tag{5.2}$$

$$\boldsymbol{T}_{ext} = C_0\boldsymbol{M}\times\boldsymbol{B}, \tag{5.3}$$

where C_0 is the constant magnetic volume of the object. We further assume the external magnetic flux density is that of a uniform rotating magnetic field given with respect to the inertial-frame basis via

$$\boldsymbol{B} = B_0\left(\cos\left(\frac{2\pi t}{T}\right)\boldsymbol{e}_x + \sin\left(\frac{2\pi t}{T}\right)\boldsymbol{e}_y\right), \tag{5.4}$$

https://doi.org/10.1017/jfm.2017.636 Published online by Cambridge University Press

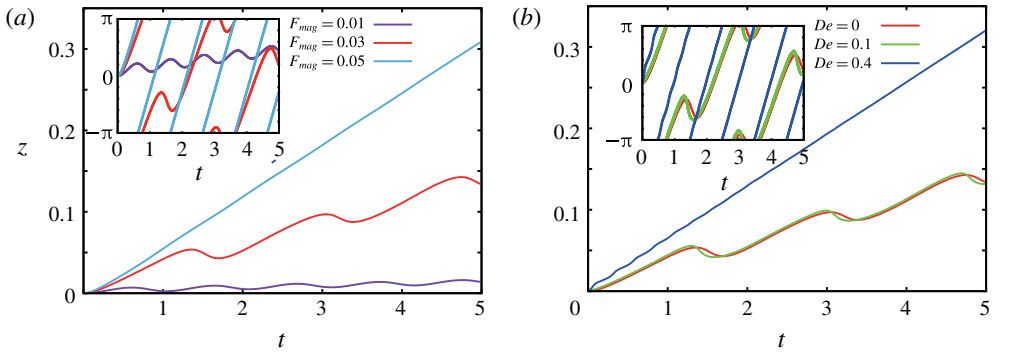


FIGURE 5. (Colour online) The dynamics of permanently magnetised swimmers. (*a*) The movement of the helical magnetic swimmer within a Newtonian fluid for a rotating magnetic flux density and varying non-dimensional magnetic torque, F_{mag}. The inset indicates the time evolution of the orientation of the swimmer magnetisation vector, as measured by θ_{mag}, the angle between $\boldsymbol{e}_x$ and $\hat{\boldsymbol{e}}_x$, measured from the x axis. (*b*) Movement of the helical magnetic swimmer with a non-dimensional magnetic torque $F_{mag} = 0.03$ in fluids with different Deborah numbers. The inset indicates the corresponding time evolution of the orientation of the magnetisation vector as in (*a*). The red curves in (*a*) and (*b*) are therefore the same.

where B_0 is constant and T is the period of rotation. Note that such fields are commonly using to guide magnetic particles (Qiu & Nelson 2015) and also that an inspection of (5.2) reveals that the magnetic force on the helix vanishes due to the spatial uniformity of the magnetic flux density.

5.2. *Computational results*

The effects of linear viscoelasticity can be treated by considering the torque balance equation. Similarly to the wall interaction case (4.4), we have

$$\int_S \epsilon_{ipq} x_p f_q^{VE} + \mathcal{L}((T_{ext})_i) = 0, \tag{5.5}$$

where we consider the linear Maxwell model, $\mathcal{L} = 1 + \lambda \partial/\partial t$, and the Deborah number is given by $De = \lambda/T$.

For the shape parameters, we set $A/L = 0.05$, $r/L = 0.003$ and $kL/2\pi = 10$, which gives the pitch of the helix to be $0.2L$. We proceed by non-dimensionalising the length, time and force scales such that in the non-dimensional model the swimmer length, time period and viscosity are given by $L = 1$, $T = 1$ and $\mu = 1$, which results in a non-dimensionalised constant representing the strength of the magnetic torque, given by $F_{mag} = C_0 M_0 B_0 (\mu L^3/T)$. We also set the initial condition of the magnetic helix so that the body-fixed frame and the inertial reference frame coincide, and we denote the origin of the body-fixed frame relative to the inertial frame by $\boldsymbol{X}(t)$. With these initial conditions, the swimmer experiences no torque at the initial time $t = 0$. The resulting boundary integral equations are analogous to those in figure 3 and are computed with $N = 366$ mesh elements and the time discretisation $\Delta t/T = 1/500$.

We first consider the motion in a Newtonian fluid, and the time evolution of the helix is plotted in figure 5(*a*) with varying non-dimensional magnetic torque, F_{mag}. The

https://doi.org/10.1017/jfm.2017.636 Published online by Cambridge University Press

plots shows the z component of the swimmer, $\boldsymbol{x} \cdot \boldsymbol{e}_z$, as a function of time, where $\boldsymbol{e}_z$ denotes the unit inertial-frame basis vector in the z direction. In the inset, the orientation of the magnetisation vector is shown via a plot of θ_{mag}, the angle between $\boldsymbol{e}_x$ and $\hat{\boldsymbol{e}}_x$, as measured from the x axis. For a sufficiently strong magnetic torque, the helix rotation is slave to that of the external field (figure 5*a* inset), and the helix moves along the z axis at constant speed. However, for weaker magnetic torques, there is a phase difference between the magnetisation vector and the external magnetic flux density. Once this phase difference exceeds π, the magnetisation vector then counter-rotates to relax to the external magnetic flux density. In turn, the helix also moves in the opposite direction, resulting in trajectories with oscillations (figure 5*a*).

We then proceed to consider non-zero Deborah number, with the same initial conditions, and focus on swimming with $F_{mag} = 0.03$, which is insufficient to induce a rotation of the helix in a constant direction within a Newtonian fluid. Analogous plots of the position and the orientation of the magnetic swimmer are shown in figure 5(*b*) with increasing Deborah numbers. When $De = 0.1$, the phase difference between the magnetisation vector and the external magnetic vector is slightly suppressed, but nonetheless is still large enough to induce counter-rotation. Further increases of the Deborah number, however, amplify the effective torque that the swimmer experiences, and result in the magnetisation vector following the external magnetic field, and thus the swimmer rotates uniformly in time, with a dramatic increase in swimming propagation.

6. Conclusions

In this paper, we have considered the dynamics of a swimmer with arbitrary prescribed deformation in a negligible Reynolds-number, non-Newtonian linear Maxwell medium. Using the Stokeslet for this medium, and introducing a generalised reciprocal relation, we have derived the boundary integral equations for linear Maxwell flows, though other linear viscoelastic flows are readily considered, as detailed in appendix A. Under the assumptions of volume-conserving deformation, the single-layer boundary integral equations are also derived, together with the force and torque balance equations. In turn this provides, to our knowledge, a first formulation of the boundary element method for a swimmer in a linear Maxwell medium that only requires surface integration. One can immediately observe that this framework demonstrates that swimming dynamics in a linear Maxwell fluid is identical to that in Newtonian Stokes flow, if no net forces and torques are acting on the swimmer. This also provides a generalisation of Purcell's scallop theorem (Purcell 1977) for Maxwell linear viscoelastic flows with arbitrary volume-conserving reciprocal motion; this result is also readily generalised to reciprocal, non-volume-conserving, deformations by including the double-layer formulation.

The exact agreement between predictions for flows and trajectories for swimmers in Newtonian media, on the one hand, and a linear Maxwell fluid, on the other, however, does break down when external forces are applied. Thus we investigated swimmer dynamics near a rigid wall, with a repulsive wall potential force acting on the swimmer, as motivated by the measurements of boundary–cell interactions by Klein *et al.* (2003), novelly incorporating the impact of linear Maxwell viscoelasticity.

Using the boundary element method provided in this paper, we thus examined swimming trajectories within a linear Maxwell viscoelastic fluid for three example swimmers: a neutral spherical tangential squirmer, a virtual bacterium and a virtual sperm. For the spherical tangential squirmer, which is scattered by hydrodynamical

https://doi.org/10.1017/jfm.2017.636 Published online by Cambridge University Press

wall interactions, the fluid viscoelasticity weakly enhances wall repulsion and affects the scattering angle. For the bacterium and sperm, which stably swim adjacent to the wall, viscoelasticity at moderate Deborah numbers does not significantly change the final stable swimming dynamics, even for the virtual sperm, which can continually experience wall interactions during a beat period while boundary swimming. Consequently we have an important null result that linear Maxwell viscoelasticity at moderate Deborah number does not alter flagellate–boundary dynamics given the waveform, even at surfaces with surface potentials. Hence our understanding of surface swimming that has been developed for Newtonian flows and standard waveforms observed from digital microscopy, as summarised in the introduction, immediately generalises. These results also support the ubiquitous simplification of using Newtonian simulation methods for sperm and bacterial motility in media well approximated by linear Maxwell viscoelasticity, such as the dilute methylcellulose solutions used as mucous analogues in sperm motility studies (Smith *et al.* 2009*b*).

As the second example case, we investigated motions of a magnetised helix under a rotating magnetic field, once more generalising to consider a linear Maxwell fluid, which demonstrated that the linear viscoelastic boundary element framework can also be applied to swimming via an external forcing as well as a prescribed shape deformation. In particular, we found that, with an intermediate strength of the magnetic induction, the model magnetic swimmer repeatedly rotates and counter-rotates within a Newtonian medium. However, in the presence of linear viscoelasticity, the swimmer is predicted to rotate at constant speed, following the external magnetic field, with a drastic increase in propagation, which illustrates that linear viscoelasticity can dramatically alter microswimmer dynamics. However, a systematic study, concerning the impact of the motion of the magnetic field, the shape of the swimmer, the details of the swimmer magnetisation and the influence of the external magnetic field, will be reported elsewhere.

Despite this example, the present framework cannot readily deal with coupled fluid–active structure problems for viscoelastic flow where the interface shape is an emergent property, since the generalisation of surface traction with viscoelasticity, that is $\boldsymbol{f}^{VE}$ in (3.21) and (3.22), does not possess a straightforward physical interpretation. Hence boundary element methods for such fluid–active structure problems in the context of linear viscoelastic fluids should be considered as a future study.

Nonetheless, the numerical techniques presented here allow one to model swimmer and particle trajectories with prescribed kinematics or external forces and torques. The framework can also readily accommodate the dynamics of small numbers of particles and swimmers via (4.3) and (4.4) for a range of linear viscoelastic constitutive laws, such as

$$\lambda\frac{\partial\boldsymbol{\tau}}{\partial t}+\boldsymbol{\tau}=2\mu\boldsymbol{D}+2\mu\gamma\frac{\partial\boldsymbol{D}}{\partial t}, \tag{6.1}$$

where $\gamma\geqslant 0$ is an additional viscoelastic response time, by noting the results in appendix A. Hence, in addition to allowing an analysis of the extent to which linear viscoelasticity impacts a diverse range of important microswimmers, as outlined here, the presented framework can be used to analyse particle–particle interactions (the underlying basis for understanding many-body effects) in active micrometre-scale linear viscoelastic rheology (Gomez-Solano & Bechinger 2015). Furthermore, any study using this linear viscoelasticity framework requires only a minimalistic generalisation of the classical boundary element method, a major advantage of the methodology.

https://doi.org/10.1017/jfm.2017.636 Published online by Cambridge University Press

Acknowledgements

K.I. is supported by JSPS-KAKENHI for Young Researchers (15H06314), Kyoto University for the Hakubi Project and Kyoto University Supporting Program for Interaction-based Initiative Team Studies (SPIRIS). K.I. acknowledges JSPS for a JSPS Overseas Research Fellowship. Elements of the simulations have been performed using the cluster computing system within the Research Institute for Mathematical Sciences (RIMS), and Institute for Information Management and Communication (IIMC), Kyoto University. The authors acknowledge anonymous referees for their comments that helped to improve the manuscript.

Appendix A. Boundary integral equations for a more general constitutive relation

Here, we derive the boundary element formulation for the more general constitutive relation,

$$\lambda\frac{\partial\boldsymbol{\tau}}{\partial t}+\boldsymbol{\tau}=:\mathcal{L}\boldsymbol{\tau}=2\mu\mathcal{M}\boldsymbol{D}:=2\mu\boldsymbol{D}+2\mu\gamma\frac{\partial\boldsymbol{D}}{\partial t}, \tag{A 1}$$

where λ and γ are viscoelastic response time scales. It is also straightforward to generalise the analysis presented here to multiple viscoelastic time scales, though we restrict ourselves to the above constitutive relation in the following.

First we require the reciprocal relation, whose derivation proceeds in the same way as in the main paper to reveal

$$\frac{\partial}{\partial x_j}((\mathcal{M}u_i')\mathcal{L}\sigma_{ij}-(\mathcal{M}u_i)\mathcal{L}\sigma_{ij}')=0. \tag{A 2}$$

We now use the viscoelastic Stokeslet satisfying $\mathcal{M}G_{ij}=G_{ij}^S$. The resulting flow due to this singularity, located at the point $\boldsymbol{x}_0$ and of strength $\boldsymbol{q}$, is governed by the relations

$$\mathcal{M}G_{ij}=G_{ij}^S \quad \text{and} \quad \mathcal{L}P_j=P_j^S, \tag{A 3a,b}$$

where the S superscript denotes the Stokes flow, Newtonian solution, with the velocity, pressure and stress fields given by

$$u_i'=\frac{1}{8\pi\mu}G_{ij}(\boldsymbol{x},\boldsymbol{x}_0)q_j, \quad p'=\frac{1}{8\pi}P_jq_j, \quad \sigma_{ij}'=\frac{1}{8\pi}T_{ijk}q_k. \tag{A 4a–c}$$

The resulting momentum-balance equation is

$$\mathcal{L}\sigma_{ij}'=-\frac{1}{8\pi}\mathcal{L}P_mq_m+\mathcal{M}D_{ij}=-\frac{1}{8\pi}P_m^Sq_m+\frac{1}{8\pi}\left(\frac{\partial G_{ip}^S}{\partial x_j}+\frac{\partial G_{jp}^S}{\partial x_i}\right)q_p=\sigma_{ij}'^S, \tag{A 5}$$

where the right-hand side is the stress tensor of a Stokes flow corresponding to a point force of strength $\boldsymbol{q}$ at the point $\boldsymbol{x}_0$. Following the derivation of the boundary integral equation in the main text, but now with the constitutive relation $\mathcal{L}\boldsymbol{\tau}=2\mu\mathcal{M}\boldsymbol{D}$, one finds

$$u_p^{VE}:=\mathcal{M}u_p(\boldsymbol{x}_0)=-\frac{1}{8\pi\mu}\int_S G_{ip}^S(\mathcal{L}\sigma_{ij})\boldsymbol{n}_j\,\mathrm{d}S+\frac{1}{8\pi}\int_S(\mathcal{M}u_i)T_{ipj}^S\boldsymbol{n}_j\,\mathrm{d}S. \tag{A 6}$$

Similarly, the single-layer boundary integral equation for a volume-preserving swimmer becomes

$$u_p^{VE}(\boldsymbol{x}_0)=-\frac{1}{8\pi\mu}\int_S G_{ip}^S(\boldsymbol{x},\boldsymbol{x}_0)f_i^{VE}(\boldsymbol{x})\,\mathrm{d}S_{\boldsymbol{x}}. \tag{A 7}$$

https://doi.org/10.1017/jfm.2017.636 Published online by Cambridge University Press

The force and torque balances remain unchanged. For instance, for the single-layer formalism, in the presence of an external wall interaction given by $\boldsymbol{f}_{wall}$, one has

$$\int_S f_i^{VE}\,\mathrm{d}S_{\boldsymbol{x}} + \mathcal{L}\int_S (f_{wall})_i\,\mathrm{d}S = 0, \quad \int_S \epsilon_{ipq}x_p f_q^{VE}\,\mathrm{d}S_{\boldsymbol{x}} + \mathcal{L}\int_S \epsilon_{ipq}x_p (f_{wall})_q\,\mathrm{d}S = 0, \quad (\mathrm{A}\,8a,b)$$

where $f_i^{VE} = \mathcal{L}(\sigma_{ij} - \sigma_{ij}^*)\boldsymbol{n}_j$, with σ_{ij}^* the stress tensor of a fictitious flow in the cell interior.

Hence to find trajectories for deformation swimming, or more generally the movement of a particle under an external force, in a linear viscoelastic fluid with the constitutive relation $\mathcal{L}\boldsymbol{\tau} = 2\mu\mathcal{M}\boldsymbol{D}$, one proceeds as in the main text, except that, at each iteration, one must also use information from the previous time point (or initial conditions at the first time step) to determine $\mathcal{M}\boldsymbol{u}(\boldsymbol{x}_0)$ in terms of the unknowns, $\boldsymbol{U}$ and $\boldsymbol{\Omega}$. The former is the velocity of a point in the body-fixed frame (the head–tail junction for simulations with bacteria and sperm is often used, for instance) and the latter is the angular velocity of the body-fixed frame relative to the inertial fixed frame around this point.

REFERENCES

BERKE, A. P., TURNER, L., BERG, H. C. & LAUGA, E. 2008 Hydrodynamic attraction of swimming microorganisms by surfaces. *Phys. Rev. Lett.* **101**, 038102.

BLAKE, J. R. 1971 A note on the image system for a Stokeslet in a no slip boundary. *Proc. Camb. Phil. Soc.* **70**, 303–310.

BOEHME, G. & MUELLER, A. 2015 Propulsion of axisymmetric swimmers in viscoelastic liquids by means of torsional oscillations. *J. Non-Newtonian Fluid Mech.* **224**, 1–16.

BRYERS, J. D. 2008 Medical biofilms. *Biotechnol. Bioengng* **100**, 1–18.

CHAUDHURY, T. K. 1979 On swimming in a viscoelastic liquid. *J. Fluid Mech.* **95**, 189–197.

CORATO, M. D., GRECO, F. & MAFFETTONE, P. L. 2015 Locomotion of a microorganism in weakly viscoelastic liquids. *Phys. Rev.* E **92**, 053008.

CURTIS, M. P. & GAFFNEY, E. A. 2013 Three-sphere swimmer in a non-linear viscoelastic medium. *Phys Rev.* E **87**, 043006.

DENISSENKO, P., KANTSLER, V., SMITH, D. J. & KIRKMAN-BROWN, J. 2012 Human spermatozoa migration in microchannels reveals boundary-following navigation. *Proc. Natl Acad. Sci. USA* **109**.

ELFRING, G. J. & GOYAL, G. 2016 The effect of gait on swimming in viscoelastic fluids. *J. Non-Newtonian Fluid Mech.* **234**, 8–14.

FENG, H., CORDOBA, A., HERNANDEZ, F., INDEI, T., LI, S., LI, X. & SCHIEBER, J. D. 2016 A boundary integral method for computing forces on particles in unsteady Stokes and linear viscoelastic fluids. *Intl J. Numer. Meth. Fluids* **82**, 198–217.

FRYMIER, P. D. & FORD, R. M. 1997 Analysis of bacterial swimming speed approaching a solid–liquid interface. *AICHE J.* **43**, 1341–1347.

FRYMIER, P. D., FORD, R. M., BERG, H. C. & CUMMINGS, P. T. 1995 Three-dimensional tracking of motile bacteria near a solid planar surface. *Proc. Natl Acad Sci. USA* **92**, 6195–6199.

FU, H. C., POWERS, T. R. & WOLGEMUTH, C. W. 2007 Theory of swimming filaments in viscoelastic media. *Phys. Rev. Lett.* **99**, 258101.

FU, H. C., WOLGEMUTH, C. W. & POWERS, T. R. 2008 Beating patterns of filaments in viscoelastic fluids. *Phys. Rev.* E **78**, 041913.

FULFORD, G. R., KATZ, D. F. & POWELL, R. L. 1998 Swimming of spermatozoa in a linear viscoelastic fluid. *Biorheology* **35**, 295–309.

FUSCO, S., ULLRICH, F., POKKI, J., CHATZIPIRPIRIDIS, G., OZKALE, B., SIVARAMAN, K. M., ERGENEMAN, O., PANE, S. & NELSON, B. J. 2014 Microrobots: a new era in ocular drug delivery. *Expert Opin. Drug Deliv.* **11**, 1815–1826.

https://doi.org/10.1017/jfm.2017.636 Published online by Cambridge University Press

GAGNON, D. A. & ARRATIA, P. E. 2016 The cost of swimming in generalized Newtonian fluids: experiments with *C. elegans*. *J. Fluid Mech.* **800**, 753–765.

GIACCHÉ, D., ISHIKAWA, T. & YAMAGUCHI, T. 2010 Hydrodynamic entrapment of bacteria swimming near a solid surface. *Phys. Rev.* E **82**, 056309.

GODINEZ, F. A., KOENS, L., MONTENEGRO-JOHNSON, T. D., ZENIT, R. & LAUGA, E. 2015 Complex fluids affect low-Reynolds number locomotion in a kinematic-dependent manner. *Exp. Fluids* **56** (5), 97.

GOMEZ, S., GODINEZ, F. A., LAUGA, E. & ZENIT, R. 2016 Helical propulsion in shear-thinning fluids. *J. Fluid Mech.* **812**, R3.

GOMEZ-SOLANO, J. R. & BECHINGER, C. 2015 Transient dynamics of a colloidal particle driven through a viscoelastic fluid. *New J. Phys.* **17**, 103032.

GOTO, T., NAKAI, T. & AOKI, K. 2010 Boundary element analysis on transition of distance and attitude of a bacterium near a rigid surface. *J. Biomech. Sci. Engng* **5**, 329–339.

GRAY, J. & HANCOCK, G. J. 1955 The propulsion of sea urchin spermatozoa. *J. Expl Biol.* **32**, 802–814.

HELANDER, H. F. & FANDRIKS, L. 2014 Surface area of the digestive tract – revisited. *Scand. J. Gastroenterol.* **49**, 681–689.

ISHIKAWA, T., SIMMONS, M. P. & PEDLEY, T. J. 2006 Hydrodynamic interaction of two-swimming model micro-organisms. *J. Fluid Mech.* **568**, 119–160.

ISHIMOTO, K., COSSON, J. & GAFFNEY, E. A. 2016 A simulation study of sperm motility hydrodynamics near fish eggs and sphere. *J. Theor. Biol.* **389**, 187–197.

ISHIMOTO, K. & GAFFNEY, E. A. 2013 Squirmer dynamics near a boundary. *Phys. Rev.* E **88**, 062702.

ISHIMOTO, K. & GAFFNEY, E. A. 2014*a* A study of spermatozoan swimming stability near a surface. *J. Theor. Biol.* **360**, 187–199.

ISHIMOTO, K. & GAFFNEY, E. A. 2014*b* Swimming efficiency of spherical squirmers: beyond the Lighthill theory. *Phys. Rev.* E **90**, 012704.

ISHIMOTO, K. & GAFFNEY, E. A. 2015 Fluid flow and sperm guidance: a simulation study of hydrodynamic sperm rheotaxis. *J. R. Soc. Interface* **12**, 20150172.

ISHIMOTO, K. & GAFFNEY, E. A. 2016 Mechanical tuning of mammalian sperm behaviour by hyperactivation, rheology and substrate adhesion: a numerical exploration. *J. R. Soc. Interface* **13**, 20160633.

ISHIMOTO, K. & YAMADA, M. 2012 A coordinate-based proof of the scallop theorem. *SIAM J. Appl. Maths* **72**, 1686–1694.

KANTSLER, V., DUNKEL, J. & GOLDSTEIN, M. P. R. E. 2013 Ciliary contact interactions dominate surface scattering of swimming eukaryotes. *Proc. Natl Acad. Sci. USA* **110**, 1187–1192.

KIM, S., LEE, S., LEE, J., NELSON, B. J., ZHANG, L. & CHOI, H. 2016 Fabrication and manipulation of ciliary microrobots with non-reciprocal magnetic actuation. *Sci. Rep.* **3**, 30713.

KLEIN, J. D., CLAPP, A. R. & DICKINSON, R. B. 2003 Direct measurement of interaction forces between a single bacterium and a flat plate. *J. Colloid Interface Sci.* **261**, 379–385.

KRIEGER, M. S., SPAGNOLIE, S. E. & POWERS, T. 2015 Microscale locomotion in a nematic liquid crystal. *Soft Matt.* **11** (47), 9115–9125.

LAUGA, E. 2009 Life at high Deborah number. *Europhys. Lett.* **86**, 64001.

LAUGA, E. 2014 Locomotion in complex fluids: integral theorems. *Phys. Fluids* **26**, 081902.

MIKI, K. & CLAPHAM, D. E. 2013 Rheotaxis guides mammalian sperm. *Curr. Biol* 443–452.

MONTENEGRO-JOHNSON, T. D., GADELHA, H. & SMITH, D. J. 2015 Spermatozoa scattering by a microchannel feature: an elastohydrodynamic model. *R. Soc. Open Sci.* **2**, doi:10.1098/rsos.140475.

NOSRATI, R., DRIOUCHI, A., YIP, C. M. & SINTON, D. 2015 Two-dimensional slither swimming of sperm within a micrometre of a surface. *Nat. Commun.* **6**, 8703.

OKABE, M. 2013 The cell biology of mammalian fertilization. *Development* **140**, 4471–4479.

PATTESON, A. E., GOPINATH, A. & ARRATIA, P. E. 2016 Active colloids in complex fluids. *Curr. Opin. Colloid Interface Sci.* **21**, 86–96.

PEDLEY, T. J. & KESSLER, J. O. 1992 Hydrodynamic phenomena in suspensions of swimming microorganisms. *Annu. Rev. Fluid Mech.* **24**, 313–358.

https://doi.org/10.1017/jfm.2017.636 Published online by Cambridge University Press

PHAN-THIEN, N. & FAN, X.-J. 2002 Viscoelastic mobility problem using a boundary element method. *J. Non-Newtonian Fluid Mech.* **105**, 131–152.

PHAN-THIEN, N., TRAN-CONG, T. & RAMIA, M. 1987 A boundary-element analysis of flagellar propulsion. *J. Fluid Mech.* **184**, 533–549.

POZRIKIDIS, C. 1992 *Boundary Integral and Singularity Methods for Linearized Viscous Flow*. Cambridge University Press.

POZRIKIDIS, C. 2002 *A Practical Guide to Boundary Element Method with Software Library BEMLIB*. CRC Press.

PURCELL, E. M. 1977 Life at low Reynolds number. *Am. J. Phys.* **45**, 3–11.

QIU, F. & NELSON, B. J. 2015 Magnetic helical micro- and nanorobots: toward thier biomedical applications. *Engineering* **1**, 21–26.

QIU, T., LEE, T.-C., MARK, A. G., MOROZOV, K. I., MÜNSTER, R., MIERKA, O., TUREK, S., LESHANSKY, A. M. & FISCHER, P. 2014 Swimming by reciprocal motion at low Reynolds number. *Nat. Commun.* **5**, 5119.

RIBET, D. & COSSART, P. 2015 How bacterial pathogens colonize their hosts and invade deeper tissues. *Microbes Infection* **17**, 173–183.

RILEY, E. E. & LAUGA, E. 2015 Small-amplitude swimmers can self-propel faster in viscoelastic fluids. *J. Theor. Biol.* **382**, 345–355.

SALAZAR, D., ROMA, A. M. & CENICEROS, H. D. 2016 Numerical study of an inextensible, finite swimmer in Stokesian viscoelastic flow. *Phys. Fluids* **28** (6).

SHUM, H., GAFFNEY, E. A. & SMITH, D. J. 2010 Modelling bacteria behaviour close to a no-slip plane boundary: the influence of bacterial geometry. *Proc. R. Soc. Lond.* A **466**, 1725–1748.

SHUM, H., TRIPATHI, A., YEOMANS, J. M. & BALAZS, A. C. 2013 Active ciliated surfaces expel model swimmers. *Langmuir* **29**, 12770–12776.

SMITH, D. J., GAFFNEY, E. A., BLAKE, J. R. & KIRKMAN-BROWN, J. C. 2009*a* Human sperm accumulation near surfaces: a simulation study. *J. Fluid Mech.* **621**, 289–320.

SMITH, D. J., GAFFNEY, E. A., GADÊLHA, H., KAPUR, N. & KIRKMAN-BROWN, J. C. 2009*b* Bend propagation in the flagella of migrating human sperm, and its modulation by viscosity. *Cell Motil. Cytoskel.* **66**, 220–236.

SPAGNOLIE, S. E. 2015 *Complex Fluids in Biological Systems*. Springer.

SPAGNOLIE, S. E. & LAUGA, E. 2012 Hydrodynamics of self-propulsion near a boundary predictions and accuracy of far-field approximations. *J. Fluid Mech.* **700**, 105–147.

SUAREZ, S. S. 2016 Mammalian sperm interactions with female reproductive tract. *Cell Tissue Res.* **363**, 185–194.

SUAREZ, S. S. & PACEY, A. A. 2006 Sperm transport in the female reproductive tract. *Hum. Reprod. Update* **12**, 23–37.

TERAN, J., FAUCI, L. & SHELLEY, M. 2010 Viscoelastic fluid response can increase the speed and efficiency of a free swimmer. *Phys. Rev. Lett.* **104**, 038101.

THOMASES, B. & GUY, R. D. 2014 Mechanisms of elastic enhancement and hindrance for finite-length undulatory swimmers in viscoelastic fluids. *Phys. Rev. Lett.* **113** (9).

XU, K., FOREST, M. G. & KLAPPER, I. 2007 On the correspondence between creeping flows of viscous and viscoelastic fluids. *J. Non-Newtonian Fluid Mech.* **145**, 150–172.

YAZDI, S., ARDEKANI, A. M. & BORHAN, A. 2014 Locomotion of microorganisms near a no-slip boundary in a viscoelastic fluid. *Phys. Rev.* E **90**, 043002.

YAZDI, S., ARDEKANI, A. M. & BORHAN, A. 2015 Swimming dynamics near a wall in a weakly elastic fluid. *J. Nonlinear Sci.* **25**, 1153–1167.

ZHANG, Z., LIU, J., MERIANO, J., RU, C., XIE, S., LUO, J. & SUN, Y. 2016 Human sperm rheotaxis: a passive physical process. *Sci. Rep.* **6**.

ZHENG, R. & PHAN-THIEN, N. 1992 A boundary element simulation of the unsteady motion of a sphere in a cylindrical tube containing a viscoelastic fluid. *Rheol. Acta* **31**, 323–332.

ZHU, L., LAUGA, E. & BRANDT, L. 2012 Self-propulsion in viscoelastic fluids: pushers versus pullers. *Phys. Fluids* **24**, 051902.

https://doi.org/10.1017/jfm.2017.636 Published online by Cambridge University Press